11 June 1998

PHYSICS LETTERS B

Physics Letters B 429 (1998) 169–187

A measurement of the inclusive $b \to s\gamma$ branching ratio

ALEPH Collaboration

R. Barate [a], D. Buskulic [a], D. Decamp [a], P. Ghez [a], C. Goy [a], J.-P. Lees [a], A. Lucotte [a], E. Merle [a], M.-N. Minard [a], J.-Y. Nief [a], B. Pietrzyk [a], R. Alemany [b], G. Boix [b], M.P. Casado [b], M. Chmeissani [b], J.M. Crespo [b], M. Delfino [b], E. Fernandez [b], M. Fernandez-Bosman [b], Ll. Garrido [b,1], E. Graugès [b], A. Juste [b], M. Martinez [b], G. Merino [b], R. Miquel [b], Ll.M. Mir [b], I.C. Park [b], A. Pascual [b], J.A. Perlas [b], I. Riu [b], F. Sanchez [b], A. Colaleo [c], D. Creanza [c], M. de Palma [c], G. Gelao [c], G. Iaselli [c], G. Maggi [c], M. Maggi [c], S. Nuzzo [c], A. Ranieri [c], G. Raso [c], F. Ruggieri [c], G. Selvaggi [c], L. Silvestris [c], P. Tempesta [c], A. Tricomi [c,2], G. Zito [c], X. Huang [d], J. Lin [d], Q. Ouyang [d], T. Wang [d], Y. Xie [d], R. Xu [d], S. Xue [d], J. Zhang [d], L. Zhang [d], W. Zhao [d], D. Abbaneo [e], U. Becker [e], P. Bright-Thomas [e], D. Casper [e], M. Cattaneo [e], V. Ciulli [e], G. Dissertori [e], H. Drevermann [e], R.W. Forty [e], M. Frank [e], R. Hagelberg [e], J.B. Hansen [e], J. Harvey [e], P. Janot [e], B. Jost [e], I. Lehraus [e], P. Mato [e], A. Minten [e], L. Moneta [e,3], A. Pacheco [e], J.-F. Pusztaszeri [e,4], F. Ranjard [e], L. Rolandi [e], D. Rousseau [e], D. Schlatter [e], M. Schmitt [e,5], O. Schneider [e], W. Tejessy [e], F. Teubert [e], I.R. Tomalin [e], H. Wachsmuth [e], Z. Ajaltouni [f], F. Badaud [f], G. Chazelle [f], O. Deschamps [f], A. Falvard [f], C. Ferdi [f], P. Gay [f], C. Guicheney [f], P. Henrard [f], J. Jousset [f], B. Michel [f], S. Monteil [f], J-C. Montret [f], D. Pallin [f], P. Perret [f], F. Podlyski [f], J. Proriol [f], P. Rosnet [f], J.D. Hansen [g], J.R. Hansen [g], P.H. Hansen [g], B.S. Nilsson [g], B. Rensch [g], A. Wäänänen [g], G. Daskalakis [h], A. Kyriakis [h], C. Markou [h], E. Simopoulou [h], I. Siotis [h], A. Vayaki [h], A. Blondel [i], G. Bonneaud [i], J.-C. Brient [i], P. Bourdon [i], A. Rougé [i], M. Rumpf [i], A. Valassi [i,6], M. Verderi [i], H. Videau [i], E. Focardi [j], G. Parrini [j], K. Zachariadou [j], M. Corden [k], C. Georgiopoulos [k], D.E. Jaffe [k], A. Antonelli [l], G. Bencivenni [l], G. Bologna [l,7], F. Bossi [l], P. Campana [l], G. Capon [l], F. Cerutti [l], V. Chiarella [l], G. Felici [l], P. Laurelli [l], G. Mannocchi [l,8], F. Murtas [l], G.P. Murtas [l], L. Passalacqua [l], M. Pepe-Altarelli [l], L. Curtis [m], A.W. Halley [m], J.G. Lynch [m], P. Negus [m], V. O'Shea [m], C. Raine [m], J.M. Scarr [m],

PII: S0370-2693(98)00404-3

K. Smith [m], P. Teixeira-Dias [m], A.S. Thompson [m], E. Thomson [m], O. Buchmüller [n], S. Dhamotharan [n], C. Geweniger [n], G. Graefe [n], P. Hanke [n], G. Hansper [n], V. Hepp [n], E.E. Kluge [n], A. Putzer [n], J. Sommer [n], K. Tittel [n], S. Werner [n], M. Wunsch [n], R. Beuselinck [o], D.M. Binnie [o], W. Cameron [o], P.J. Dornan [o,9], M. Girone [o], S. Goodsir [o], E.B. Martin [o], N. Marinelli [o], A. Moutoussi [o], J. Nash [o], J.K. Sedgbeer [o], P. Spagnolo [o], M.D. Williams [o], V.M. Ghete [p], P. Girtler [p], E. Kneringer [p], D. Kuhn [p], G. Rudolph [p], A.P. Betteridge [q], C.K. Bowdery [q], P.G. Buck [q], P. Colrain [q], G. Crawford [q], A.J. Finch [q], F. Foster [q], G. Hughes [q], R.W.L. Jones [q], N.A. Robertson [q], T. Sloan [q], M.I. Williams [q], I. Giehl [r], A.M. Greene [r], C. Hoffmann [r], K. Jakobs [r], K. Kleinknecht [r], G. Quast [r], B. Renk [r], E. Rohne [r], H.-G. Sander [r], P. van Gemmeren [r], C. Zeitnitz [r], J.J. Aubert [s], C. Benchouk [s], A. Bonissent [s], G. Bujosa [s], J. Carr [s,9], P. Coyle [s], F. Etienne [s], O. Leroy [s], F. Motsch [s], P. Payre [s], M. Talby [s], A. Sadouki [s], M. Thulasidas [s], K. Trabelsi [s], M. Aleppo [t], M. Antonelli [t], F. Ragusa [t], R. Berlich [u], W. Blum [u], V. Büscher [u], H. Dietl [u], G. Ganis [u], H. Kroha [u], G. Lütjens [u], C. Mannert [u], W. Männer [u], H.-G. Moser [u], S. Schael [u], R. Settles [u], H. Seywerd [u], H. Stenzel [u], W. Wiedenmann [u], G. Wolf [u], J. Boucrot [v], O. Callot [v], S. Chen [v], A. Cordier [v], M. Davier [v], L. Duflot [v], J.-F. Grivaz [v], Ph. Heusse [v], A. Höcker [v], A. Jacholkowska [v], D.W. Kim [v,10], F. Le Diberder [v], J. Lefrançois [v], A.-M. Lutz [v], M.-H. Schune [v], E. Tournefier [v], J.-J. Veillet [v], I. Videau [v], D. Zerwas [v], P. Azzurri [w], G. Bagliesi [w,9], G. Batignani [w], S. Bettarini [w], T. Boccali [w], C. Bozzi [w], G. Calderini [w], M. Carpinelli [w], M.A. Ciocci [w], R. Dell'Orso [w], R. Fantechi [w], I. Ferrante [w], L. Foà [w,11], F. Forti [w], A. Giassi [w], M.A. Giorgi [w], A. Gregorio [w], F. Ligabue [w], A. Lusiani [w], P.S. Marrocchesi [w], A. Messineo [w], F. Palla [w], G. Rizzo [w], G. Sanguinetti [w], A. Sciabà [w], G. Sguazzoni [w], R. Tenchini [w], G. Tonelli [w,12], C. Vannini [w], A. Venturi [w], P.G. Verdini [w], G.A. Blair [x], L.M. Bryant [x], J.T. Chambers [x], M.G. Green [x], T. Medcalf [x], P. Perrodo [x], J.A. Strong [x], J.H. von Wimmersperg-Toeller [x], D.R. Botterill [y], R.W. Clifft [y], T.R. Edgecock [y], S. Haywood [y], P.R. Norton [y], J.C. Thompson [y], A.E. Wright [y], B. Bloch-Devaux [z], P. Colas [z], S. Emery [z], W. Kozanecki [z], E. Lançon [z,9], M.-C. Lemaire [z], E. Locci [z], P. Perez [z], J. Rander [z], J.-F. Renardy [z], A. Roussarie [z], J.-P. Schuller [z], J. Schwindling [z], A. Trabelsi [z], B. Vallage [z], S.N. Black [aa], J.H. Dann [aa], R.P. Johnson [aa], H.Y. Kim [aa], N. Konstantinidis [aa], A.M. Litke [aa], M.A. McNeil [aa], G. Taylor [aa], C.N. Booth [ab], C.A.J. Brew [ab], S. Cartwright [ab], F. Combley [ab], M.S. Kelly [ab], M. Lehto [ab], J. Reeve [ab], L.F. Thompson [ab], K. Affholderbach [ac], A. Böhrer [ac], S. Brandt [ac], G. Cowan [ac], C. Grupen [ac], P. Saraiva [ac], L. Smolik [ac], F. Stephan [ac], G. Giannini [ad],

B. Gobbo [ad], G. Musolino [ad], J. Rothberg [ae], S. Wasserbaech [ae], S.R. Armstrong [af], E. Charles [af], P. Elmer [af], D.P.S. Ferguson [af], Y. Gao [af], S. González [af], T.C. Greening [af], O.J. Hayes [af], H. Hu [af], S. Jin [af], P.A. McNamara III [af], J.M. Nachtman [af,13], J. Nielsen [af], W. Orejudos [af], Y.B. Pan [af], Y. Saadi [af], I.J. Scott [af], J. Walsh [af], Sau Lan Wu [af], X. Wu [af], G. Zobernig [af]

[a] *Laboratoire de Physique des Particules (LAPP), IN2P3-CNRS, F-74019 Annecy-le-Vieux Cedex, France*
[b] *Institut de Física d'Altes Energies, Universitat Autònoma de Barcelona, E-08193 Bellaterra (Barcelona), Spain [14]*
[c] *Dipartimento di Fisica, INFN Sezione di Bari, I-70126 Bari, Italy*
[d] *Institute of High-Energy Physics, Academia Sinica, Beijing, People's Republic of China [15]*
[e] *European Laboratory for Particle Physics (CERN), CH-1211 Geneva 23, Switzerland*
[f] *Laboratoire de Physique Corpusculaire, Université Blaise Pascal, IN2P3-CNRS, Clermont-Ferrand, F-63177 Aubière, France*
[g] *Niels Bohr Institute, DK-2100 Copenhagen, Denmark [16]*
[h] *Nuclear Research Center Demokritos (NRCD), GR-15310 Attiki, Greece*
[i] *Laboratoire de Physique Nucléaire et des Hautes Energies, Ecole Polytechnique, IN2P3-CNRS, F-91128 Palaiseau Cedex, France*
[j] *Dipartimento di Fisica, Università di Firenze, INFN Sezione di Firenze, I-50125 Firenze, Italy*
[k] *Supercomputer Computations Research Institute, Florida State University, Tallahassee, FL 32306-4052, USA [17,18]*
[l] *Laboratori Nazionali dell'INFN (LNF-INFN), I-00044 Frascati, Italy*
[m] *Department of Physics and Astronomy, University of Glasgow, Glasgow G12 8QQ, United Kingdom [19]*
[n] *Institut für Hochenergiephysik, Universität Heidelberg, D-69120 Heidelberg, Germany [20]*
[o] *Department of Physics, Imperial College, London SW7 2BZ, United Kingdom [19]*
[p] *Institut für Experimentalphysik, Universität Innsbruck, A-6020 Innsbruck, Austria [21]*
[q] *Department of Physics, University of Lancaster, Lancaster LA1 4YB, United Kingdom [19]*
[r] *Institut für Physik, Universität Mainz, D-55099 Mainz, Germany [20]*
[s] *Centre de Physique des Particules, Faculté des Sciences de Luminy, IN2P3-CNRS, F-13288 Marseille, France*
[t] *Dipartimento di Fisica, Università di Milano e INFN Sezione di Milano, I-20133 Milano, Italy*
[u] *Max-Planck-Institut für Physik, Werner-Heisenberg-Institut, D-80805 München, Germany [20]*
[v] *Laboratoire de l'Accélérateur Linéaire, Université de Paris-Sud, IN2P3-CNRS, F-91405 Orsay Cedex, France*
[w] *Dipartimento di Fisica dell'Università, INFN Sezione di Pisa, e Scuola Normale Superiore, I-56010 Pisa, Italy*
[x] *Department of Physics, Royal Holloway & Bedford New College, University of London, Surrey TW20 OEX, United Kingdom [19]*
[y] *Particle Physics Dept., Rutherford Appleton Laboratory, Chilton, Didcot, Oxon OX11 OQX, United Kingdom [19]*
[z] *CEA, DAPNIA / Service de Physique des Particules, CE-Saclay, F-91191 Gif-sur-Yvette Cedex, France [22]*
[aa] *Institute for Particle Physics, University of California at Santa Cruz, Santa Cruz, CA 95064, USA [23]*
[ab] *Department of Physics, University of Sheffield, Sheffield S3 7RH, United Kingdom [19]*
[ac] *Fachbereich Physik, Universität Siegen, D-57068 Siegen, Germany [20]*
[ad] *Dipartimento di Fisica, Università di Trieste e INFN Sezione di Trieste, I-34127 Trieste, Italy*
[ae] *Experimental Elementary Particle Physics, University of Washington, Seattle, WA 98195, USA*
[af] *Department of Physics, University of Wisconsin, Madison, WI 53706, USA [24]*

Received 30 March 1998
Editor: L. Montanet

Abstract

The flavour changing neutral current decay $b \to s\gamma$ has been detected in hadronic Z decays collected by ALEPH at LEP. The signal is isolated in lifetime-tagged $b\bar{b}$ events by the presence of a hard photon associated with a system of high momentum and high rapidity hadrons. The background processes are normalised from the data themselves. The inclusive branching ratio is measured to be

$$\left(3.11 \pm 0.80_{\mathrm{stat}} \pm 0.72_{\mathrm{syst}}\right) \times 10^{-4},$$

consistent with the Standard Model expectation via penguin processes.

1. Introduction

The flavour changing neutral current decay $b \to s\gamma$ may proceed via an electromagnetic penguin diagram in which the photon is radiated from either the W or one of the quark lines. The next-to-leading order calculations are now available for this transition [1] and the Standard Model predicts the inclusive $b \to s\gamma$ branching ratio to be $(3.51 \pm 0.32) \times 10^{-4}$ for measurements at the $\Upsilon(4S)$ resonance and $(3.76 \pm 0.30) \times 10^{-4}$ at the Z peak [2]. Virtual particles in the loop may be replaced by non-Standard Model particles, such as charged Higgs bosons or supersymmetric particles. These additional contributions could either enhance or suppress the decay rate [3,4] making it sensitive to physics beyond the Standard Model.

The $b \to s\gamma$ process is expected to be dominated by two-body (resonant) decays such as $B \to K^*\gamma$, and final states with soft gluon emission (non-resonant) which kinematically resemble two-body decays [5,6]. In this case, the photon energy in the b-hadron rest frame, denoted $E_\gamma^\star$, has a spectrum which is peaked at approximately half the b-hadron mass. In contrast, charged current radiative b decays such as $b \to cW^*\gamma$ and $b \to uW^*\gamma$ (where W^* represents a virtual W boson) produce photons with a spectrum resembling that from bremsstrahlung and hence of much lower energy [7]. The decay $b \to d\gamma$ can also be mediated by penguin diagrams but is Cabibbo suppressed, with a predicted branching ratio $\leq 2.8 \times 10^{-5}$ [8]. In the ALEPH data sample of 4.1 million hadronic Z decays, collected between 1991 and 1995, the Standard Model predicts the production of ~ 660 $b \to s\gamma$ decays. It is thus important, if a $b \to s\gamma$ signal is to be observed, that both the signal acceptance and background rejection be high and that $E_\gamma^\star$ be accurately reconstructed. The latter requires precise determination of the parent b-hadron's momentum and direction.

In the analyis described in this paper, $b\bar{b}$ events are tagged by lifetime in one hemisphere. The signal for the $b \to s\gamma$ decay in the other hemisphere is characterised by the presence of a hard photon associated with a system of high momentum and high rapidity hadrons, originating from a displaced secondary vertex. The extraction of the signal is based on a Monte Carlo simulation constructed using Heavy Quark Effective Theory [5], and from measurements and assumptions about exclusive decay rates.

[1] Permanent address: Universitat de Barcelona, 08208 Barcelona, Spain.
[2] Also at Dipartimento di Fisica, INFN, Sezione di Catania, Catania, Italy.
[3] Now at University of Geneva, 1211 Geneva 4, Switzerland.
[4] Now at School of Operations Research and Industrial Engineering, Cornell University, Ithaca, NY 14853-3801, USA.
[5] Now at Harvard University, Cambridge, MA 02138, USA.
[6] Supported by the Commission of the European Communities, contract ERBCHBICT941234.
[7] Also Istituto di Fisica Generale, Università di Torino, Torino, Italy.
[8] Also Istituto di Cosmo-Geofisica del C.N.R., Torino, Italy.
[9] Also at CERN, 1211 Geneva 23, Switzerland.
[10] Permanent address: Kangnung National University, Kangnung, Korea.
[11] Now at CERN, 1211 Geneva 23, Switzerland.
[12] Also at Istituto di Matematica e Fisica, Università di Sassari, Sassari, Italy.
[13] Now at University of California at Los Angeles (UCLA), Los Angeles, CA 90024, USA.
[14] Supported by CICYT, Spain.
[15] Supported by the National Science Foundation of China.
[16] Supported by the Danish Natural Science Research Council.
[17] Supported by the US Department of Energy, contract DE-FG05-92ER40742.
[18] Supported by the US Department of Energy, contract DE-FC05-85ER250000.
[19] Supported by the UK Particle Physics and Astronomy Research Council.
[20] Supported by the Bundesministerium für Bildung, Wissenschaft, Forschung und Technologie, Germany.
[21] Supported by Fonds zur Förderung der wissenschaftlichen Forschung, Austria.
[22] Supported by the Direction des Sciences de la Matière, C.E.A.
[23] Supported by the US Department of Energy, grant DE-FG03-92ER40689.
[24] Supported by the US Department of Energy, grant DE-FG0295-ER40896.

2. The ALEPH detector

A detailed description of the ALEPH detector and its performance is given in [9,10]. What follows is a brief description of those parts of the detector relevant to this analysis. Charged particles are detected in the central part of the detector, consisting of a high precision vertex detector (VDET), a cylindrical multi-wire drift chamber (ITC) and a large time projection chamber (TPC). The VDET consists of two concentric layers of double sided silicon detectors surrounding the beam pipe, positioned at average radii of 6.5 and 10.8 cm covering 85% and 69% of the solid angle, respectively. The intrinsic spatial resolution of the VDET is 12 μm for the $r-\phi$ coordinate and between 11 and 22 μm for the z coordinate, depending on the polar angle of the charged particle. The ITC, at radii from 16 to 26 cm, provides up to eight coordinates per track in the $r-\phi$ view while the TPC measures up to 21 three-dimensional points per track at radii between 40 and 171 cm. The TPC also serves to separate charged particle species with up to 338 measurements of their specific ionization. The three detectors are immersed in an axial magnetic field of 1.5 T and together provide a transverse momentum resolution of $\sigma(1/p_T) = 0.6 \times 10^{-3}$ (GeV/c)$^{-1}$ for high momentum tracks.

Electrons and photons are identified and measured in the electromagnetic calorimeter (ECAL) which is formed by a barrel surrounding the TPC, closed at each end by end-cap modules. It consists of 45 layers of lead interleaved with proportional wire chambers. The position and energies of electromagnetic showers are measured using cathode pads each subtending a solid angle of 0.9° by 0.9° in θ and ϕ and connected internally to form projective towers. Each tower is read out in three segments, known as storeys, with depths of 4, 9 and 9 radiation lengths. The inactive zones of this detector represent 2% of the solid angle in the barrel and 6% in the end-caps. The iron return yoke of the magnet is instrumented with streamer tubes to form a hadron calorimeter (HCAL), with a thickness of over 7 interaction lengths. It is surrounded by two additional double layers of streamer tubes used for muon identification.

An energy flow algorithm, which is described in [10], is used to improve the energy resolution of events. The algorithm links charged tracks to calorimeter clusters and uses the resultant redundancy in energy measurements to assign neutral particle energy. Particle identification methods are used in this algorithm to distinguish between particle species and the resulting objects are labelled energy flow objects. The algorithm to identify photons in ECAL is also described in detail in [10]. The clusters found by the algorithm are retained as candidate photons if their energy is greater than 0.25 GeV and there is no charged track impact at a distance of less than 2 cm from the cluster barycentre. The photons are detected with angular resolution of $\sigma_{\theta,\phi} = (2.5/\sqrt{E(\mathrm{GeV})} + 0.25)$ mrad and energy resolution of $\sigma_E/E = (0.25/\sqrt{E(\mathrm{GeV})} + 0.009)$. The detector's ability to resolve a π^0 into two γ clusters decreases for energies greater than 10 GeV above which the two γ clusters overlap to form one larger cluster which tends to be more elliptical than single γ clusters. A moments analysis of the energy sharing between neighbouring detector elements within the cluster enables the length of the major axis of the shower ellipse, σ_l, to be measured. This quantity is used in the analysis which follows to separate high energy π^0 mesons ($\sigma_l > 2.3$ cm) from single photons ($\sigma_l < 2.3$ cm).

3. Monte Carlo simulation

Monte Carlo events were generated using JETSET [11] with the ALEPH standard parameter set. These events were processed through a detailed simulation of the ALEPH detector and the ALEPH reconstruction program. A sample of 9.9 million hadronic Z decays — simulated without the $b \to s\gamma$ decay and henceforth called the *standard* Monte Carlo — is used to model background processes in this analysis. The rate of production of photons from final state radiation (FSR) in the standard MC is reweighted by a factor 1.21 as required by the ALEPH measurements of this process over the full kinematic range [12].

The composition of the signal ($b \to s\gamma$) Monte Carlo event sample is based primarily on predictions from Heavy Quark Effective Theory for the exclusive ratios $R_{K^{**}} = \Gamma(B \to K^{**}\gamma)/\Gamma(B \to X_s\gamma)$, where K^{**} is

Table 1
The composition of the inclusive b → sγ Monte Carlo sample

Exclusive decay channel	Exclusive decay fraction, R(%)
$B_{u(d)} \to K^*(892)\gamma$	13.6 ± 5.1
$B_{u(d)} \to K_1(1270)\gamma$	5.5 ± 2.1
$B_{u(d)} \to K_1(1400)\gamma$	7.2 ± 2.6
$B_{u(d)} \to K^*(1410)\gamma$	6.7 ± 2.6
$B_{u(d)} \to K_2^*(1430)\gamma$	20.6 ± 7.5
$B_{u(d)} \to K(n\pi)\gamma$	22.0 ± 19.9
	⇒ 75.6
$B_s \to \phi(1020)\gamma$	2.0 ± 0.8
$B_s \to h_1(1380)\gamma$	0.8 ± 0.3
$B_s \to f_1(1420)\gamma$	1.1 ± 0.4
$B_s \to \phi(1680)\gamma$	1.0 ± 0.4
$B_s \to f_2'(1525)\gamma$	3.0 ± 1.1
$B_s \to KK(n\pi)\gamma$	3.3 ± 3.0
	⇒ 11.2
$\Lambda_b \to \Lambda(1116)\gamma$	13.2 ± 4.1

any particular K-resonance and the B meson is either a B_u or B_d [5]. $R_{K^*(892)}$ is taken as the ratio of the CLEO measurements of the exclusive $B \to K^*(892)\gamma$ branching ratio [13] and the inclusive $b \to s\gamma$ branching ratio [14], giving $R_{K^*(892)} = 18.1 \pm 6.8\,\%$. The ϕ-resonances, produced in B_s penguin decays, are assumed to be in the same relative proportions as the K-resonances. The exclusive ratios for resonant decays are summed and the remaining inclusive branching ratio is completed with non-resonant penguin decays, where X_s is a multi-body state involving a kaon and n pions, hadronised using JETSET. The photon energy spectrum in the non-resonant decays is obtained from a fully inclusive spectator model including gluon bremsstrahlung and higher order radiative effects [6]. The model parameters used were $m_q = 150\ \mathrm{MeV}/c^2$, where m_q is the spectator quark mass, and $p_F = 265\ \mathrm{MeV}/c$, where p_F is the Fermi momentum of the b quark in the hadron, taken from CLEO fits to the inclusive lepton spectrum in $B \to Xl\nu$ decays [15]. Baryonic penguins are modelled by one channel, $\Lambda_b \to \Lambda\gamma$, where the Λ_b is produced directly from hadronisation or from the decay of a heavier b baryon. The resulting signal Monte Carlo composition is shown in Table 1, where the b-hadron production fractions are taken to be: $B_{u(d)}$ 75.6%; B_s 11.2%; and Λ_b 13.2% [16].

4. Inclusive reconstruction of $b \to s\gamma$ decays

The event hemisphere opposite to a $b \to s\gamma$ decay contains a typical b-hadron decay and is used to 'b-tag' events in a largely unbiased way. The $b \to s\gamma$ hemisphere, in contrast, has low multiplicity, a single displaced decay vertex, and contains a high energy photon. A dedicated inclusive $b \to s\gamma$ reconstruction algorithm is used to assemble the hadronic system accompanying the photon by distinguishing between objects from the b-hadron decay from those produced by hadronisation at the primary vertex.

In each hemisphere containing a candidate photon, π^0 and K_S^0 mesons are searched for. The π^0 mesons are reconstructed from two candidate photons when the $\gamma\gamma$ invariant mass is compatible with the π^0 mass. K_S^0 mesons are reconstructed similarly from any two oppositely signed charged tracks which form a vertex and have an invariant mass (assuming both charged tracks are pions) consistent with the K_S^0 mass. Each hemisphere then consists of reconstructed π^0 and K_S^0 mesons and the remaining charged tracks and neutral electromagnetic and hadronic clusters. Any neutral hadronic cluster is assumed to be a K_L^0 and given the kaon mass. All charged tracks are given the pion mass and, depending on the length of the major axis of its shower ellipse, σ_l, a neutral electromagnetic cluster is given either zero mass (photon) or the pion mass (unresolved π^0).

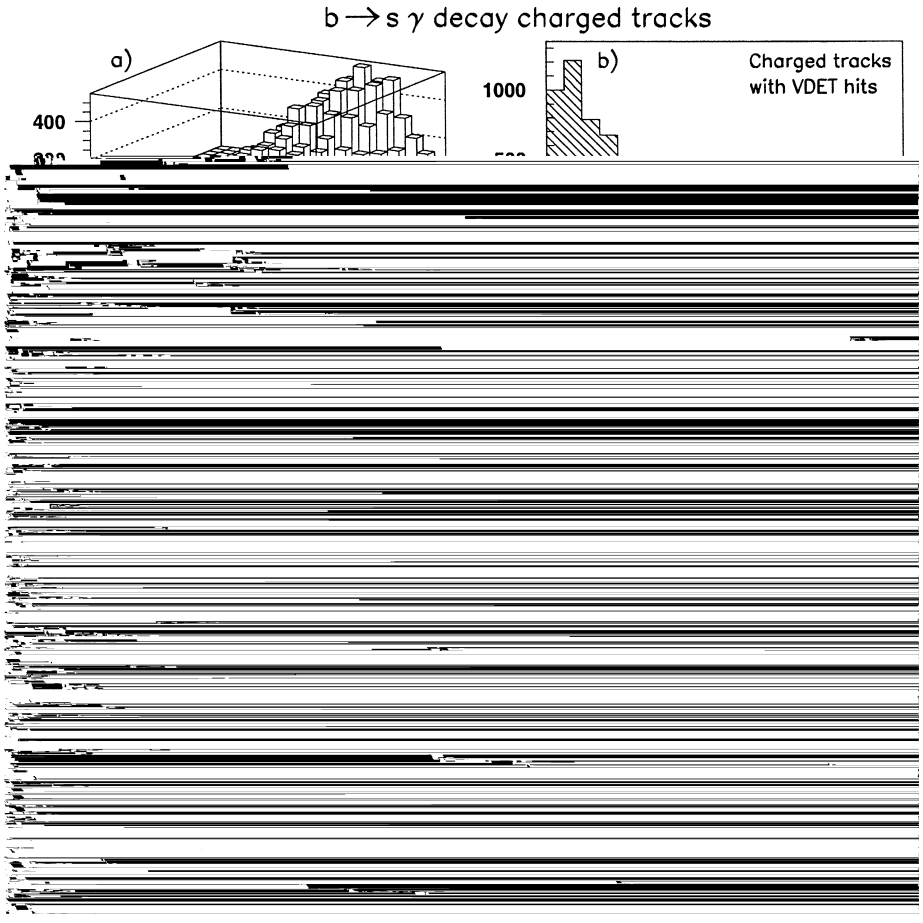

Fig. 1. The momentum-rapidity (a) and impact parameter significance (b) distributions for signal charged tracks and the corresponding hadronisation charged track distributions (c) and (d). Plot (e) shows the momentum probability distribution in the rapidity bin, 2.5 < rapidity < 2.75, and (f) shows the total charged track impact parameter significance probability distribution. The curves in (e) and (f) are the fitted parameterisations.

The $b \to s\gamma$ probability for each object is calculated as a function of its momentum, its rapidity with respect to the b-hadron direction, and, if the object is a charged track with VDET hits, its three-dimensional impact parameter significance. The probability functions were produced using signal Monte Carlo events. Plots (a) and (b) of Fig. 1 show the momentum-rapidity and impact parameter significance distributions for charged tracks from the $b \to s\gamma$ decay. Plots (c) and (d) of Fig. 1 show the corresponding hadronisation charged track distributions. The $b \to s\gamma$ decay objects have a much harder momentum spectrum than the hadronisation objects and possess larger rapidities. Similarly, due to the long lifetime of the b-hadron, the signal objects have more significant impact parameters than the hadronisation objects, where the spectrum is dominated by the impact parameter resolution. In a given momentum bin the $b \to s\gamma$ probability, P_{mom}, is defined as:

$$P_{mom} = \frac{\text{No. of } b \to s\gamma \text{ decay objects}}{\text{No. of } b \to s\gamma \text{ decay objects} + \text{No. of hadronisation objects}}$$

If the object is a charged track with VDET hits, the independent impact parameter significance probability is

calculated in the same way as P_{mom} and the two probabilities, P_{mom} and P_{ip}, are combined to give a final probability, P:

$$P = \frac{P_{mom} \cdot P_{ip}}{P_{mom} \cdot P_{ip} + (1 - P_{mom}) \cdot (1 - P_{ip}) \cdot r}$$

where r is the average ratio of the total number of signal decay charged tracks with VDET hits to the total number of hadronisation charged tracks with VDET hits in a $b \to s\gamma$ hemisphere ($r = 0.298$). Fig. 1(e) shows the momentum probability distribution in the rapidity bin, $2.5 < \text{Rapidity} < 2.75$, and Fig. 1(f) shows the charged track impact parameter significance probability distribution.

The momentum probability functions are constructed for ten different rapidity bins which are used to interpolate to the probability corresponding to any value of rapidity and momentum. The probabilities are calculated separately for identified K_L^0 and K_S^0 mesons and all other objects, since kaons from the $b \to s\gamma$ decay have a harder momentum spectrum than other X_s decay products and can therefore be separated from hadronisation kaons more easily.

These probability functions are used in the jet reconstruction algorithm now described. The reconstruction of an assumed $b \to s\gamma$ decay begins with the candidate signal photon onto which objects (K_S^0 and π^0 mesons, charged tracks and neutral calorimeter objects) in the same hemisphere as the photon are added in order of decreasing $b \to s\gamma$ probability. The addition of objects stops if, by adding the next highest probability object, the mass of the reconstructed jet is further from the mean B meson mass of 5.28 GeV/c^2 than it would be if the object had not been added. This reconstruction is performed in two stages, as follows:

1. An initial estimate of the b-hadron flight direction is obtained by using only those objects with rapidity with respect to the thrust axis greater than 1.0 and then calculating the probabilities as a function of momentum and impact parameter significance only.
2. The 4-momenta of the candidate photon and its accompanying high rapidity objects are then summed and used as a new estimate of the b-hadron flight direction with which a better estimate of the object rapidities can be made. The above process is then repeated but with the rapidity cut removed and the momentum probability function replaced by a 2-dimensional momentum-rapidity probability function.

The resulting jets are accepted as possible $b \to s\gamma$ decays if the jet mass is within 0.7 GeV/c^2 of the mean B meson mass of 5.28 GeV/c^2; the mass of the hadronic system, X_s, is less than 4.0 GeV/c^2; and the X_s object multiplicity (K_S^0 and π^0 mesons, charged tracks and neutral calorimeter objects) is greater than one and less than eight. After this procedure, studies of the signal Monte Carlo show that $b \to s\gamma$ decays are well reconstructed with a resolution in momentum of 1.5 GeV/c and angle of 0.3° [17].

5. Event selection and data analysis

A sample of 4.06 million hadronic Z decays is preselected according to the standard ALEPH hadronic event selection [10]. To ensure the event is well contained within the detector volume, the cosine of the polar angle of the thrust axis is required to be less than 0.9, where the thrust axis is determined using all energy flow objects. To allow the calculation of variables used to tag b events, jets are reconstructed using the JADE algorithm [18] with a y_{cut} of 0.02, where each event must have at least one track with VDET hits and a minimum of two jets with momentum greater than 10 GeV/c and polar angle greater than 5.7° [19].

A set of cuts is used to produce a data sample enriched in $b \to s\gamma$ events. To reduce the background from π^0 decays, events are selected with at least one electromagnetic cluster containing a single candidate photon of energy more than 10 GeV that cannot be combined with another candidate photon to make an invariant mass of less than 0.2 GeV/c^2. The hemisphere opposite to the candidate photon is required to be b-like with P_{hem}^{opp} less than 0.1, where P_{hem}^{opp} is the probability that all charged tracks in the hemisphere are consistent with having

Table 2
Predicted efficiencies for each of the exclusive $b \to s\gamma$ decay channels after the background rejection cuts. The uncertainties are the Monte Carlo statistical uncertainties. The $b \to s\gamma$ efficiency is the average of the exclusive channels weighted by their production rates, as given in Table 1. The final two columns give the means and standard deviations of the exclusive E_γ^* spectra, after all the cuts described in section 5

Decay channel	Efficiency (%)	$< E_\gamma^* >$ (GeV)	σ (GeV)
$B_{u(d)} \to K^*(892)\gamma$	14.5 ± 0.5	2.49	0.19
$B_{u(d)} \to K_1(1270)\gamma$	15.0 ± 0.6	2.42	0.17
$B_{u(d)} \to K_1(1400)\gamma$	13.5 ± 0.5	2.39	0.18
$B_{u(d)} \to K^*(1410)\gamma$	13.0 ± 0.5	2.38	0.18
$B_{u(d)} \to K_2^*(1430)\gamma$	13.8 ± 0.5	2.39	0.18
$B_{u(d)} \to K(n\pi)\gamma$	12.4 ± 0.4	2.37	0.21
$B_s \to \phi(1020)\gamma$	17.7 ± 1.7	2.52	0.15
$B_s \to h_1(1380)\gamma$	14.7 ± 1.5	2.40	0.19
$B_s \to f_1(1420)\gamma$	14.0 ± 1.5	2.38	0.19
$B_s \to \phi(1680)\gamma$	13.0 ± 1.7	2.36	0.21
$B_s \to f_2'(1525)\gamma$	12.1 ± 1.4	2.41	0.15
$B_s \to KK(n\pi)\gamma$	13.5 ± 1.1	2.34	0.21
$\Lambda_b \to \Lambda(1116)\gamma$	7.4 ± 0.4	2.45	0.23
$b \to s\gamma$	12.8 ± 0.3	2.41	0.20

originated from the reconstructed primary vertex [19]. In the Monte Carlo the hemisphere probabilities are corrected using the impact parameter smearing algorithm described in [20] which improves the agreement between data and Monte Carlo. In the remaining events, jets are reconstructed and selected as described in Section 4, and the decay objects — including the photon — are transformed into the rest frame of their parent jet. The angle of the photon, $\theta_\gamma^\star$, in this frame relative to the jet direction, is required to have $\cos\theta_\gamma^\star$ less than 0.55 since $\cos\theta_\gamma^\star$ peaks at unity for background processes whereas photons are emitted isotropically in $b \to s\gamma$ decays. Furthermore, the boosted sphericity, S_b, in the jet's rest frame [21] is required to be less than 0.16, because this quantity is peaked at zero for two-body $b \to s\gamma$ decays but has a broad distribution for background processes.

The expected efficiencies for the various exclusive $b \to s\gamma$ channels after all these cuts are shown in Table 2 along with the means and standard deviations of their reconstructed E_γ^* spectra. From the original data sample, 1560 hadronic Z decays remain, each containing only one candidate photon (two events with more than one candidate photon were rejected). The expectation from the background Monte Carlo is 1443 events with a single candidate photon of which 34% are π^0 mesons from $b \to c$ decays; 30% are π^0 mesons from non-b decays; 13% are prompt photons from $(q \to q\gamma)$ final state radiation (FSR) of which 23% are from light (uds) quarks, 53% are from c quarks and 24% are from b quarks; 17% are photons from other (non-FSR) sources, half of which are from η decays; 4% are π^0 mesons from $b \to u$ decays; and the remaining 2% are of undetermined origin (because there is no one-to-one correspondence between the reconstructed objects and ''true'' simulated particles).

The final sample of 1560 hadronic events is split into eight sub-samples, defined in Table 3. The $b \to s\gamma$ decay populates mainly sub-sample 4. Dividing the data up in this way allows the relative normalisations of the remaining background processes to be measured outside the signal region.

The first four sub-samples have $\sigma_l < 2.3$ cm and hence have candidate photons resembling prompt photons while the second set of sub-samples have $\sigma_l > 2.3$ cm and are π^0-like, see Fig. 2 (a). The data are further divided into sub-samples of relatively high or low b-purity, containing jets of relatively high or low energy, by binning in $-\log P_{hem}^{opp}$ and E_{jet} respectively. This is done to separate signal photons from FSR photons and to distinguish between π^0 mesons produced in b hadron decays and other (non-b) π^0 mesons, see Fig. 2 (b,c).

Table 3
Defining the sub-samples, where $f_{b\to s\gamma}$ in column 5 is the fraction of $b\to s\gamma$ decays populating each sub-sample and E_{jet} is the energy of the reconstructed $b\to s\gamma$ candidates

Sub-sample	E_{jet}(GeV)	$-\log P_{hem}^{opp}$	σ_l(cm)	$f_{b\to s\gamma}$(%)		
1	< 32	1.2 – 2.2	< 2.3	8.4	γ-like	low b-purity
2	32 – 50	1.2 – 2.2	< 2.3	19.2	”	”
3	< 32	> 2.2	< 2.3	17.1	”	high b-purity
4	32 – 50	> 2.2	< 2.3	47.0	”	”
5	< 32	1.2 – 2.2	> 2.3	0.7	π^0-like	low b-purity
6	32 – 50	1.2 – 2.2	> 2.3	2.8	”	”
7	< 32	> 2.2	> 2.3	1.1	”	high b-purity
8	32 – 50	> 2.2	> 2.3	3.7	”	”

The $E_\gamma^\star$ distributions for the eight subsamples are shown in Fig. 3 together with the background Monte Carlo (dashed curve) which is absolutely normalised.

The background Monte Carlo gives a reasonable representation of the data, but there is an excess where the $b\to s\gamma$ signal is expected (sub-sample 4 in the range 2.2 GeV $< E_\gamma^* <$ 2.8 GeV). Due to the $b\to s\gamma$ reconstruction algorithm, background events in which the jet contains a FSR photon tend to produce peaks in the $E_\gamma^\star$ spectrum in the vicinity of the $b\to s\gamma$ signal region. From Monte Carlo studies it is found that the residual FSR $E_\gamma^\star$ peaks are most prominent in sub-samples 1 and 3, and are almost absent in sub-samples 2 and 4 where the signal is greatest. Thus, uncertainty in the FSR rate does not cause significant uncertainty in the number of background events in the $b\to s\gamma$ signal region. To measure the uncertainties in the background levels, and improve the agreement of the Monte Carlo and the data, a multivariate fit is performed where the normalisation of the four major backgrounds and the $b\to s\gamma$ signal rate are allowed to be free parameters.

A binned log-likelihood fit of the $E_\gamma^\star$ data distributions is performed for the eight sub-samples using the corresponding distributions for the signal and background simulations, and the HMCMML fitting package [22] which correctly incorporates uncertainties due to the finite Monte Carlo statistics in each bin. The five parameters in the fit are $N_{b\to s\gamma}$, N_{FSR}, $N_{(b\to c)\pi^0}$, $N_{(\mathrm{non}-b)\pi^0}$ and N_{other}, which are, respectively, the total number of signal, FSR, $(b\to c)\pi^0$, $(\mathrm{non}-b)\pi^0$, and ‘other’ background events which make up the remaining data. The shapes of the $E_\gamma^\star$ distributions are taken from the standard Monte Carlo. The sensitivity of the fit to $b\to s\gamma$ enters mainly through sub-sample 4 where there is little FSR expected and, according to Monte Carlo the b purity is 96.6%.

6. Results

6.1. Extraction of the $b\to s\gamma$ signal

The results of the multivariate fit are shown in Table 4. A significant amount of $b\to s\gamma$ is required to fit the data while the adjustments of the background normalisations lead to an improved agreement between data and the background Monte Carlo. These adjustments are within the accuracy of the fit for N_{other}, N_{FSR} and $N_{(\mathrm{non}-b)\pi^0}$ as would be expected from previous ALEPH measurements [12,23]. However, significant modification is required to the $(b\to c)\,\pi^0$ normalisation. This is not unexpected since there is a 50% uncertainty in the branching ratio for such decays [16]. The correlation matrix for the fit is shown in Table 5.

The $E_\gamma^\star$ plots for the sub-samples are shown in Fig. 3 for data and Monte Carlo before and after the fit. Before the fit, the χ^2 is 87.1 for 68 degrees of freedom and after the fit the χ^2 is 66.6 for 63 degrees of freedom — where, in both cases, only bins with at least four entries are included in the χ^2 calculation. Fig. 4

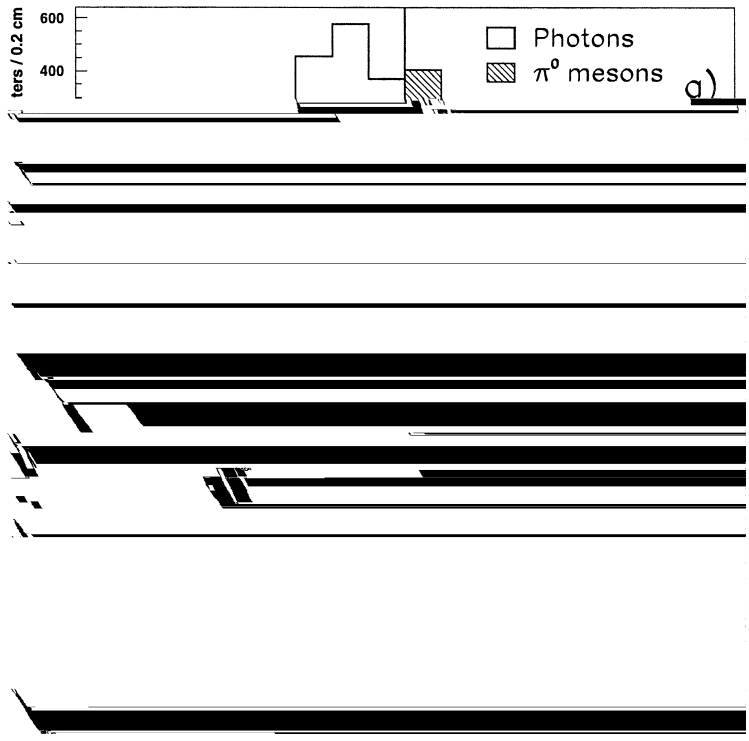

Fig. 2. Monte Carlo distributions for the quantities used to define the sub-samples. The vertical lines at $\sigma_l = 2.3$ cm, $E_{jet} = 32$ GeV and $-\log P_{hem}^{opp} = 2.2$ define the eight event sub-samples, as in Table 3.

shows the improved agreement between data and Monte Carlo after the fit in each of the main variables used in the analysis, both in the event selection and the fit itself. These distributions are dominated by background processes and this agreement indicates that the shapes of the backgrounds are well modelled in the Monte Carlo, in the selected range.

Fig. 5 (a) shows the E_γ^* distribution for sub-sample 4 in data and Monte Carlo after the normalisations of the background processes have been corrected for. The remaining excess after subtraction of the background is seen in Fig. 5 (b) with the fitted signal distribution superimposed. The shape of this distribution is consistent with the observed excess within statistical uncertainties indicating a signal for $b \to s\gamma$. If the fit is repeated with $N_{b \to s\gamma}$ constrained to zero, the excess distribution shown in Fig. 5 (b) remains almost the same. The reason for this is that the background is mainly constrained by the data outside the signal region (2.2 GeV $< E_\gamma^* <$ 2.8 GeV in sub-sample 4) and is hardly influenced by the data in the signal region. The excess in Fig. 5 (b) is thus demonstrated to be insensitive to the details of the fit.

6.2. Consistency checks of the $b \to s\gamma$ hypothesis

For the purest sample of $b \to s\gamma$ events (sub-sample 4) and in the signal region (2.2 GeV $< E_\gamma^\star <$ 2.8 GeV) there is evidence in the remaining data events, after subtraction of the corrected background, of lifetime in the *same* hemisphere as the photon. This is consistent with that expected from $b \to s\gamma$, see Fig. 6(a,b).

In the signal region of sub-sample 4 there is seen to be an excess of high momentum kaons, that is strangeness, in the data which is again consistent with $b \to s\gamma$, see Fig. 6(c,d). Charged kaons are required to have ionisation in the TPC within one standard deviation of the kaon hypothesis and greater than two standard

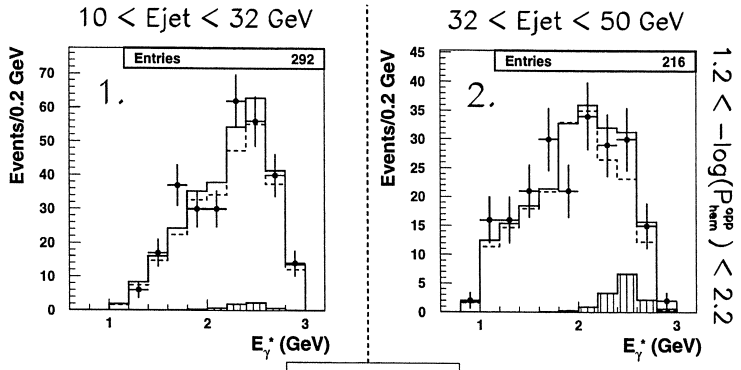
10 < Ejet < 32 GeV
32 < Ejet < 50 GeV
Entries 292
Entries 216
1.
2.
Events/0.2 GeV
E_γ^* (GeV)
$1.2 < -\log(P_{hem}^{opp}) < 2.2$

Table 4
Results of the five parameter fit to the data

Fit parameter	Standard (normalised) MC value	Fitted value	Change in value (%)
N_{other}	336.8 ± 11.7	390.7 ± 66.0	+16 ± 20
N_{FSR}	223.0 ± 10.5	239.6 ± 36.5	+7 ± 16
$N_{(non-b)\pi^0}$	431.8 ± 13.3	507.7 ± 78.6	+18 ± 18
$N_{(b\to c)\pi^0}$	482.0 ± 14.0	352.7 ± 59.1	−27 ± 12
$N_{b\to s\gamma}$	0	69.4 ± 19.7	–

Table 5
Correlation matrix for the five parameter fit

	N_{other}	N_{FSR}	$N_{(non-b)\pi^0}$	$N_{(b\to c)\pi^0}$	$N_{b\to s\gamma}$
N_{other}	1	−0.20	−0.45	−0.23	−0.03
N_{FSR}	–	1	−0.27	0.27	−0.37
$N_{(non-b)\pi^0}$	–	–	1	−0.54	0.12
$N_{(b\to c)\pi^0}$	–	–	–	1	−0.18
$N_{b\to s\gamma}$	–	–	–	–	1

deviations away from either the electron or pion hypothesis while the identification of K_L^0 and K_S^0 mesons was described in Section 4. The data distribution contains 38 kaon candidates (20 K_L^0 mesons, 11 K_S^0 mesons and 7 charged kaons). After the fit the Monte Carlo predicts a background of 20 kaons (9.9 K_L^0 mesons, 3.4 K_S^0 mesons and 6.8 charged kaons) and a signal of 16.2 kaons (5.4 K_L^0 mesons, 5.0 K_S^0 mesons, and 5.8 charged kaons).

Finally, on combining sub-samples 4 and 8 for the $E_\gamma^\star$ signal region, the excess σ_l distribution (Fig. 6(e)) peaks at about 2 cm which is characteristic of single photons (which have $<\sigma_l> = 1.991 \pm 0.007$ cm) rather than π^0 mesons (which have $<\sigma_l> = 2.251 \pm 0.034$ cm). This is well modelled by the fitted signal Monte Carlo, as shown in Fig. 6(f). The mean σ_l for data (2.062 ± 0.033 cm) tends to be photon-like, and is 3.0 standard deviations less than the mean σ_l for the background Monte Carlo (2.187 ± 0.026 cm) which consists mainly of π^0 decays. Hence the excess is not consistent with a fluctuation of the π^0 background.

6.3. The inclusive $b \to s\gamma$ branching ratio.

These observations show that the excess in Fig. 5 is photon-like and tends to have a lifetime distribution and a strangeness content consistent with the $b \to s\gamma$ process. This evidence supports the hypothesis that the excess is due to $b \to s\gamma$ decays. The inclusive $b \to s\gamma$ branching ratio is then evaluated as follows:

$$Br(b \to s\gamma) = \frac{N_{b\to s\gamma}}{\varepsilon_{b\to s\gamma}} \cdot \frac{1}{2\, N_{had}\, R_b}$$

where $\varepsilon_{b\to s\gamma}$ is the efficiency with which inclusive $b \to s\gamma$ decays pass the event selection and is given in Table 2; N_{had} is the number of hadronic Z decays in the data after the standard ALEPH hadronic event

Fig. 3. The $E_\gamma^\star$ distributions in data (error bars) and the Monte Carlo (histograms) before and after the fit for the eight sub-samples. The dashed histogram is the standard Monte Carlo (no $b \to s\gamma$) before the fit. The solid histogram is the Monte Carlo (including $b \to s\gamma$) after the fit. The shaded histogram is the $b \to s\gamma$ contribution from the fitted Monte Carlo.

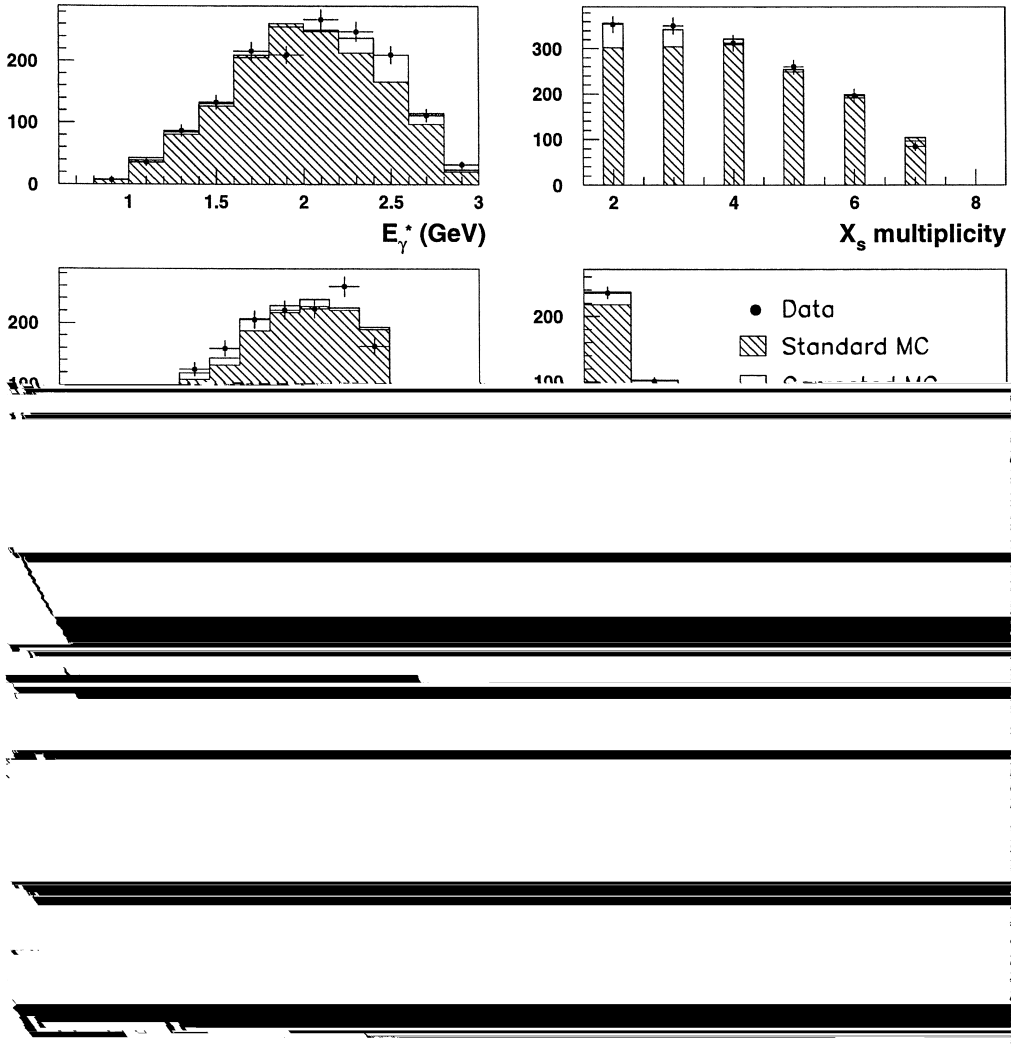

Fig. 4. Comparing data and Monte Carlo events before (standard MC) and after (corrected MC) the fit in each cut variable and fit variable.

selection; and R_b is the $Z \rightarrow b\bar{b}$ hadronic branching fraction which is set to its Standard Model value of 0.2158 [25]. The resulting branching ratio and its total statistical uncertainty is:

$$Br(b \rightarrow s\gamma) = (3.11 \pm 0.88) \times 10^{-4}.$$

7. Statistical and systematic uncertainties

Table 6 gives a breakdown of the statistical and systematic uncertainties on the branching ratio measurement. The methods used to evaluate these uncertainties are described below, where each uncertainty is referred to by its label in the table.

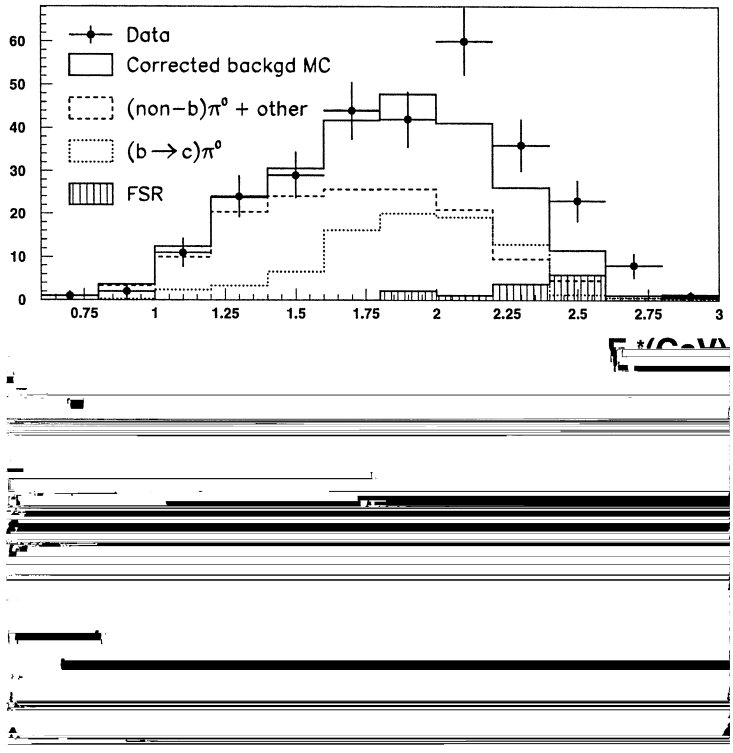

Fig. 5. The energy of the photon in the rest frame of the reconstructed jet. The top figure shows the data and Monte Carlo background events in sub-sample 4 (see section 5), after the correction of the background processes' relative normalisations. The bottom figure shows the excess in data after subtraction of the corrected Monte Carlo background and the signal distribution resulting from the multivariate fit. Also shown is the excess remaining in the data when a fit is performed without $b \to s\gamma$.

The total $Br(b \to s\gamma)$ fit uncertainty (Δ_{fit}) has a small contribution, Δ_1, from the $b \to s\gamma$ Monte Carlo statistics. The covariance matrix produced in the fit is used to extract the uncertainties in the branching ratio for $b \to s\gamma$ due to uncertainties in the four other parameters in the fit by adopting the method described in [24], giving a combined systematic uncertainty of Δ_2. The background normalisation uncertainty (Δ_2) is added in quadrature to the signal Monte Carlo statistical uncertainty (Δ_1), and the remaining uncertainty in Δ_{fit} is assumed to be the statistical uncertainty on $Br(b \to s\gamma)$ due to the finite *data* statistics (Δ_{stat}). As the fit results give a background Monte Carlo composition which is different from the standard ALEPH Monte Carlo, a conservative systematic uncertainty (Δ_3) is evaluated as follows. The $b \to s\gamma$ branching ratio is recalculated using the standard Monte Carlo prediction for the background normalisations and allowing only $N_{b \to s\gamma}$ to vary in the fit; then Δ_3 is taken to be the difference between this branching ratio and the value derived in Section 6. The χ^2 for this one parameter fit is 72.4 for 67 degrees of freedom.

The accuracy of the fit depends on how well the Monte Carlo represents the shape of the data in $E_\gamma^\star$ and on the relative proportion of each background source in each sub-sample. The systematic uncertainty due to a possible imprecision of the Monte Carlo in this regard is assessed by observing the change in the measured branching ratio as the boundaries between the eight sub-samples are varied. In this way it is possible to vary the background in the signal region leaving the signal itself approximately unchanged. For example, as the E_{jet} boundary is decreased it is possible to increase the FSR background by up to a factor 3 and the other backgrounds by a factor 2 leaving the signal approximately constant in sub-samples 2 and 4. Similarly increasing the σ_l boundary allows the other backgrounds to increase by up to a factor of 1.7 leaving the FSR

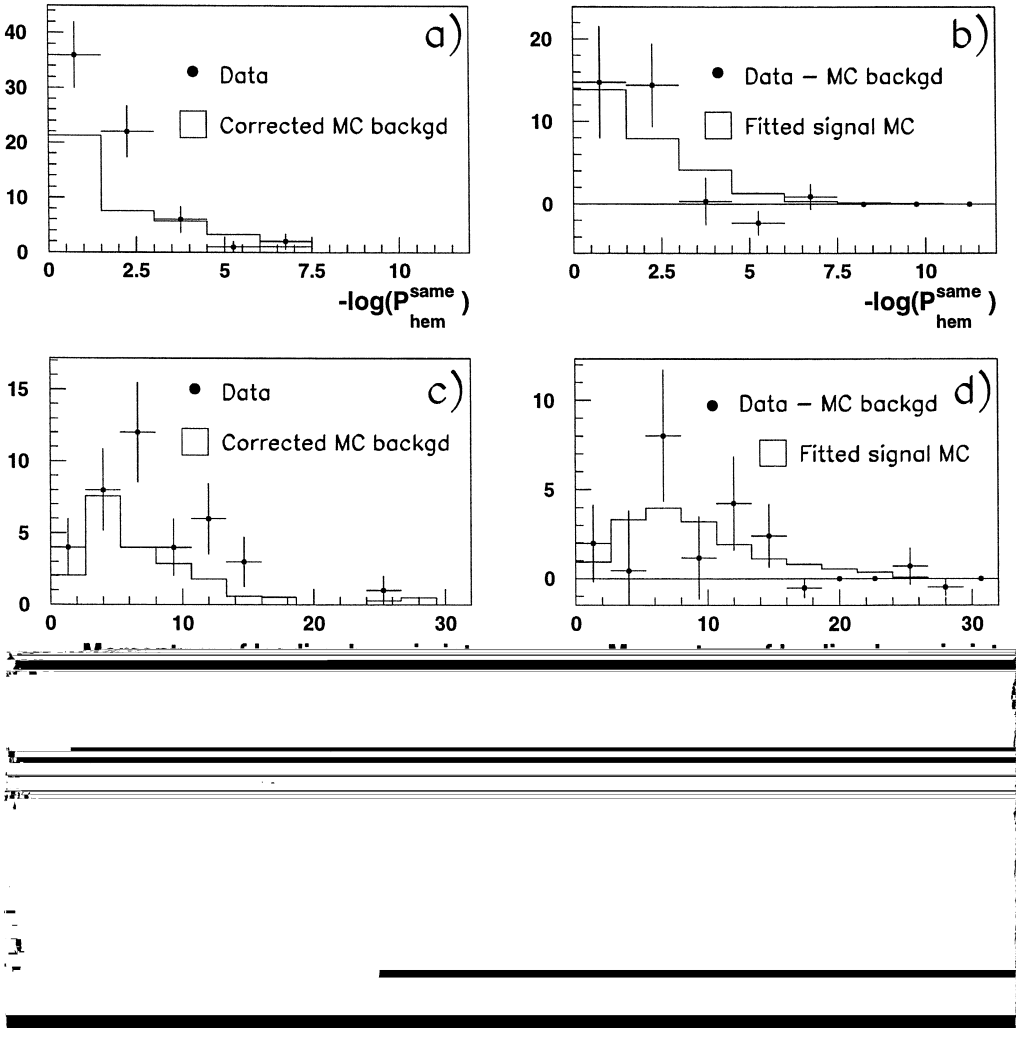

Fig. 6. Supporting evidence for the $b \to s\gamma$ signal: (a) displays the impact parameter hemisphere probability in the same hemisphere as the candidate photon for data and the corrected background Monte Carlo, while the excess of data above the background, along with the fitted signal distribution, are shown in (b); (c) and (d) show the leading kaon momentum distributions for data, background Monte Carlo and signal Monte Carlo; (e) and (f) show the shower major axis length distributions for data, background Monte Carlo and signal Monte Carlo. The events are selected as described in the text.

and the signal in regions 2 and 4 almost unchanged. As these changes are made the branching ratio changes by Δ_4 and this is taken as a systematic uncertainty, although such changes are compatible with statistical fluctuations. The branching ratio measurement is found to be insensitive to variation of the cut values in the other variables, $\cos\theta_\gamma^\star$, S_b, E_γ and $-\log P_{hem}^{opp}$ [17].

The total jet energy (E_{jet}) for candidate b hadrons is obtained by adding the energies contributing to the jet of the charged tracks ($\sim 30\%$ of the total energy on average); all neutral hadronic clusters which are assumed to be K_L^0 ($\sim$ 4% on average); and electromagnetic clusters ($\sim 66\%$ on average). For those jets (1% of the total) which lie between $\cos\theta$ of 0.9 and 0.95 relative to the beam axis, where there are uncertain energy losses due to imperfections in the detector coverage at these small angles, the calibration uncertainty is taken to be 10%. For

Table 6
Uncertainties on the Br($b \to s\gamma$) measurement. Note that $\Delta_{\rm fit}$ is the total statistical uncertainty which comes from the multivariate fit

	Source of uncertainty	Uncertainty ($\times 10^{-4}$)
Δ_1	Signal Monte Carlo statistics	0.065
Δ_2	Background Monte Carlo statistics	0.376
Δ_3	Background Monte Carlo composition	0.185
Δ_4	Background shapes	0.462
Δ_5	Energy calibration uncertainties	0.182
Δ_6	K_L^0 detection efficiency	0.031
Δ_7	σ_1 scale	0.097
	0.200	
Δ_{11}	B meson production fractions	0.012
Δ_{12}	b quark Fermi momentum	0.028
Δ_{13}	Assumption for $B_s \to X_{s\bar{s}}\gamma$ exclusive branching fractions	0.014
$\Delta_{\rm stat}$	Data statistics –- $\Delta_{\rm stat} = \sqrt{\Delta_{fit}^2 - \Sigma_{i=1}^2 \Delta_i^2}$	0.80
$\Delta_{\rm sys}$	Total systematic uncertainty $= \sqrt{\Sigma_{i=1}^{13} \Delta_i^2}$	0.72
$\Delta_{\rm tot}$	Total uncertainty $= \sqrt{\Delta_{stat}^2 + \Delta_{sys}^2}$	1.08

the remaining jets, the calibration uncertainty of the energy scale is taken to be 1.0% and is obtained by weighting the calibration uncertainty of the ECAL (1.5%), the HCAL (4%) and charged tracks (0.2%) by the average fraction of the energy in each, as given above. Varying E_{jet} within these uncertainties, for the appropriate events, results in a shift in the fitted branching ratio of Δ_5. The uncertainty in the HCAL detection efficiency for K_L^0 mesons in HCAL is taken to be 4% and since this affects a quarter of $b \to s\gamma$ decays it corresponds to a 1% systematic uncertainty on the branching ratio (Δ_6).

A fit to the σ_l data distribution using Monte Carlo background π^0 mesons and photons, for which the mean σ_l values are allowed to vary in the fit, results in a negligible shift in the mean σ_l for photons but a $(+1.6 \pm 0.8)$% shift for π^0 mesons. The change in the $b \to s\gamma$ branching ratio measurement when the σ_l scale is increased by 1.6% for Monte Carlo π^0 mesons is Δ_7.

The remaining systematic uncertainties are evaluated by reweighting signal and background Monte Carlo events to take into account modelling uncertainties, repeating the fit, and measuring the resultant changes in the branching ratio measurement. The $b \to u$ decay rate used in the fit (1.5%) is varied over the range of its uncertainty ($\pm$ 50%), giving a shift in the measurement of Δ_8. The systematic uncertainty due to theoretical uncertainty in the relative fractions of *exclusive* penguin decays in the *inclusive* $b \to s\gamma$ model (Δ_9) is calculated by repeating the fit with two extreme signal Monte Carlo compositions. Firstly the fractions of resonant penguins are all increased to their upper limits — as shown in Table 1 — while the numbers of non-resonant penguins are reduced to compensate; then the fractions of resonant penguins are all decreased to their lower limits while the numbers of non-resonant penguins are increased to compensate. The fit is also repeated with the fraction of baryonic $b \to s\gamma$ decays set to zero, giving a shift of Δ_{10}. The production fractions of B mesons are varied within their experimental limits [16] to give a combined uncertainty of Δ_{11}. The central Fermi momentum value used in the simulation of $B \to K(n\pi)$, 265 MeV, is changed by its uncertainty, ± 25 MeV [15], which gives a maximum shift of Δ_{12}. Finally, a systematic uncertainty of Δ_{13} is evaluated to account for the assumption that the exclusive B_s penguin decays are produced in the same relative fractions as the exclusive $B_{u(d)}$ penguin decays by measuring the effect of weighting the B_s penguin decay branching fractions according to their spin multiplicity [26] instead of those given in Table 1.

8. Conclusions

The inclusive $b \to s\gamma$ branching ratio is measured to be:

$$\left(3.11 \pm 0.80_{\text{stat}} \pm 0.72_{\text{syst}}\right) \times 10^{-4}.$$

This could include a small contribution from $b \to d\gamma$. The result is consistent with both the Standard Model prediction of $(3.76 \pm 0.30) \times 10^{-4}$ [2] and the only previous measurement of $(2.32 \pm 0.57 \pm 0.35) \times 10^{-4}$ by CLEO [14]. The L3 [27] and DELPHI [28] collaborations at LEP have previously performed searches for radiative charmless b decays and placed 90% confidence level upper limits of 1.2×10^{-3} and 5.4×10^{-4}, respectively, on the branching ratio.

Acknowledgements

We wish to congratulate our colleagues in the CERN accelerator divisions for the excellent performance of the LEP machine. We are grateful to the engineers and technicians at all the collaborating institutions for their contribution to the success of ALEPH. Those of us from non-member states are grateful to CERN for its hospitality. We would like to thank A. Ali, T. Ohl and M. Neubert for helpful discussions, C. Greub for providing us with a $b \to s\gamma$ spectator model program, and R. Poling for explaining the CLEO method for determining the b quark Fermi momentum.

References

[1] K. Chetyrkin et al., Phys. Lett. B 400 (1997) 206; C. Greub, T. Hurth, $B \to X_s\gamma$ in the Standard Model, hep-ph/9708214, 1997; A.J. Buras et al., Phys. Lett. B 414 (1997) 157.
[2] A. Ali, Theory of rare B decays, DESY 97-192, to be published in the Proceedings of the Seventh International Symposium on Heavy Flavor Physics, Santa Barbara, California, 1997.
[3] J.L. Hewett, Phys. Rev. Lett. 70 (1993) 1045.
[4] A.J. Buras et al., Nucl. Phys. B 424 (1994) 374.
[5] A. Ali et al., Phys. Lett. B 298 (1993) 195; private communications with A. Ali.
[6] A. Ali, C. Greub, Phys. Lett. B 259 (1991) 182; private communications with C. Greub.
[7] A. Ali, C. Greub, Phys. Lett. B 293 (1992) 226.
[8] A. Ali, Nucl. Phys. (Proc. Suppl.) 59 (1997) 86.
[9] ALEPH Collaboration, Nucl. Instr. and Meth. A 294 (1990) 121.
[10] ALEPH Collaboration, Nucl. Instr. and Meth. A 360 (1995) 481.
[11] T. Sjöstrand, Comp. Phys. Comm. 82 (1994) 74.
[12] ALEPH Collaboration, Z. Phys. C 57 (1993) 17; C 69 (1996) 365.
[13] CLEO Collaboration, Radiative penguin decays of the B meson, CLEO CONF 96-05, Contributed paper to the International Conference on High Energy Physics, Warsaw, 1996.
[14] CLEO Collaboration, Phys. Rev. Lett. 74 (1995) 2885.
[15] R. Wang, Measurements of the inclusive semileptonic branching fraction of B mesons at the Upsilon (4S) resonance, Ph.D. thesis, University of Minnesota, 1994.
[16] Particle Data Group, Phys. Rev. D 54 (1996).
[17] M.I. Williams, A measurement of the inclusive branching ratio for $b \to s\gamma$ with the ALEPH detector at LEP, Ph.D. thesis, RAL-TH-97-019, University of Lancaster, 1997.
[18] JADE Collaboration, Z. Phys. C 33 (1986) 23.
[19] ALEPH Collaboration, Phys. Lett. B 313 (1993) 535.
[20] ALEPH Collaboration, Phys. Lett. B 401 (1997) 150.
[21] TASSO Collaboration, Phys. Lett. B 149 (1984) 524.
[22] R. Barlow, C. Beeston, Comp. Phys. Comm. 77 (1993) 219.
[23] ALEPH Collaboration, Z. Phys. C 74 (1997) 451; Phys. Rept. 294 (1998).

[24] F. James, MINUIT, CERN program library long writeup D 506 (1994), Section 7.3.1.
[25] D. Bardin, W. Hollik, G. Passarino (Eds.), Precision calculations for the Z resonance, Report CERN-95-03, 1995.
[26] Private communications with T. Ohl.
[27] L3 Collaboration, Phys. Lett. B 317 (1993) 637.
[28] DELPHI Collaboration, Z. Phys. C 72 (1996) 207.